All-optical Stückelberg spectroscopy of strongly driven Rydberg states

Ulrich Bengs,[1] Serguei Patchkovskii,[1] Misha Ivanov,[1,2,3] and Nickolai Zhavoronkov[1,*]
[1]*Max-Born Institut Berlin, Max-Born Strasse 2A, 12489 Berlin, Germany*
[2]*Department of Physics, Humboldt University, Newtonstraße 15, 12489 Berlin, Germany*
[3]*Blackett Laboratory, Imperial College London, London SW7 2AZ, United Kingdom*

(Received 20 October 2021; accepted 24 March 2022; published 19 May 2022)

The AC Stark shift of electronic levels is ubiquitous in the interaction of intense light fields with atoms and molecules. As the light intensity changes on the rising and falling edges of a femtosecond laser pulse, it shifts the Rydberg states in and out of multiphoton resonances with the ground state. The two resonant pathways for transient excitation arising at the leading and the trailing edges of the pulse generate Young's type interference, generally referred to as the Stückelberg oscillations. Here we report the observation of the Stückelberg oscillations in the intensity of the coherent free-induction decay following resonant multiphoton excitation. Moreover, combining the experimental results with accurate numerical simulations and a simple model, we use the Stückelberg oscillations to recover the population dynamics of strongly driven Rydberg states inside the laser pulse by all-optical measurements after the end of the pulse. We demonstrate the potential of this spectroscopy to characterize lifetimes of Rydberg states dressed by laser fields with strengths far exceeding the Coulomb field between the Rydberg electron and the core.

DOI: 10.1103/PhysRevResearch.4.023135

The formation of electronically highly excited states—both transient, existing only in the presence of the strong electromagnetic field, and long-lived—is a key process underlying much of atomic and molecular strong-field physics [1]. Recombination of the transient, strongly driven excited states yields extreme ultraviolet (EUV) to soft x-ray emission, presenting not only a practically important light source with unique properties but also containing rich information on the structure and dynamics of the target atom or molecule, forming the basis of high-harmonic spectroscopy (HHS) [1,2]. An important aspect of the strong-field interaction are the multiphoton resonances mediated by the ubiquitous Rydberg states, dubbed "Freeman resonances" [3–7], later re-emerging as "frustrated tunneling" in infrared fields (see, e.g., Refs. [8–12]).

Such resonances are inevitable as the field-dressed Rydberg states experience the AC Stark shift, which mostly follows the ponderomotive potential U_p of the laser field and exceeds the laser photon energy in strong laser fields, generally leading to resonances on the rising and the falling edges of the laser pulse [Fig. 1(a)].

As the resonance occurs twice, the two pathways must interfere, leading to intensity-dependent oscillations in the population of excited states and ion yield [6,13], known as Stückelberg oscillations. They were first predicted for atomic collisions nearly a century ago [14] and arise whenever a transient resonance condition re-appears after a well-defined time interval. They have been observed in a variety of contexts, from microwave ionization of Rydberg atoms [15] to Ramsey-type interference in three-photon ionization of Na [13], to one-photon ionization by x-ray fields [16,17].

This mechanism is the foundation for Landau-Zener-Stückelberg interferometry (see e.g., [18] for a recent overview). Yet, the Stückelberg oscillations have never been observed for the simplest and ubiquitous strong-field atomic process: the multiphoton Rydberg-state excitation (see, e.g., Ref. [6]).

The purpose of this paper is twofold. First, we show that an all-optical measurement of the free-induction decay (FID) emission is a sensitive all-optical probe of the coherent, long-lived population of Rydberg states prepared by an intense laser pulse, and that the all-optical setup allows one to control the volume-averaging effects and reveal the Stückelberg oscillations hidden underneath. Second, we show how one can use this Ramsey-type Stückelberg interferometer as a delicate probe of the dynamics and decay of strongly driven Rydberg states inside the driving laser pulse. We confirm our experimental observations and our spectroscopic proposal through accurate numerical simulations. Unless noted otherwise, atomic units $\hbar = m_e = |e| = 1$ are used throughout.

The key idea of the Stückelberg spectroscopy is detailed in Fig. 1(a). It relies on observing the Stückelberg oscillations while changing the peak laser intensity. A laser-dressed Rydberg state passes through a multiphoton resonance with the ground state on the leading (instant t_1) and falling (instant t_2) edges of the pulse. For a symmetric laser pulse and negligible ground-state depletion, the two excitation amplitudes are identical. However, the Rydberg population excited at the

*zhavoron@mbi-berlin.de

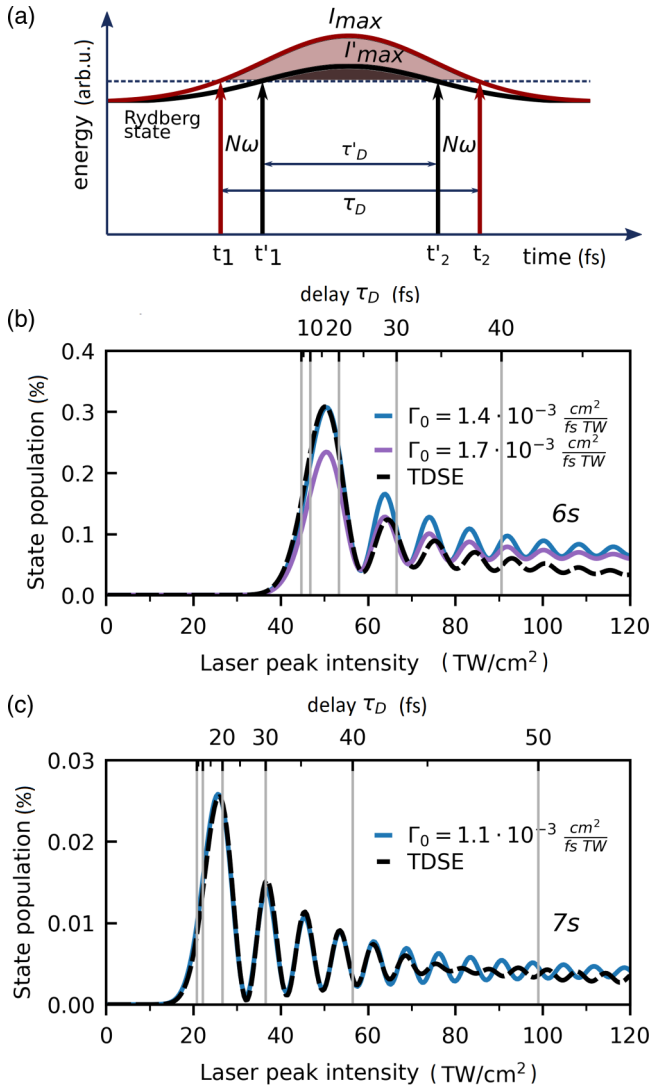

FIG. 1. (a) Origin of the Stückelberger oscillations. Energy of the Rydberg state follows the instantaneous field intensity I. (b), (c) Populations of the 6s and 7s states in Argon as a function of laser intensity in the TDSE calculation and the simplified two-level atom model (see text for details). The upper axis shows the time delay between two resonance events [see panel (a)].

pulse front (instant t_1) may be depleted between t_1 and t_2. This depletion affects the interference, which can therefore be used to characterize the depletion. Specifically, the Rydberg-state population w at the end of the laser pulse (time T) is [6,19]

$$w(I_{\max}) \propto e^{-\int_{t_2}^{T}\Gamma(t)dt}\left|e^{-\frac{1}{2}\int_{t_1}^{t_2}\Gamma(t)dt - i\phi(t_2,t_1)} + 1\right|^2. \quad (1)$$

Here $\phi(t_2, t_1)$ is the relative phase between the two transition amplitudes accumulated between t_1 and t_2 [the colored areas in Fig. 1(a); see Ref. [19] for details]; $\exp(-\frac{1}{2}\int_{t_1}^{t_2}\Gamma(t)dt)$ describes the loss of the Rydberg state amplitude due to ionization between t_1 and t_2. Thus, measuring the Stückelberg oscillations vs the laser intensity gives access to the behavior of strongly driven Rydberg states, both their amplitude and the phase, including their stability against ionization in intense laser fields. The maxima (minima) of the oscillations, which occur when $\phi(t_2, t_1)$ is an even (odd) multiple of π, measure the phase accumulated by the strongly driven Rydberg state between the resonances. For the ponderomotive Stark shift and well separated t_1 and t_2, the maxima appear at intensities separated by [19]

$$\Delta I_{\max} \approx 4B_0\omega^2\frac{2\pi}{\tau_{\rm FWHM}}, \quad (2)$$

where ω is the driver carrier frequency and $\tau_{\rm FWHM}$ is the laser pulse duration, $\frac{2\pi}{\tau_{\rm FWHM}}$ is approximately the bandwidth of the laser pulse, and $B_0 \simeq 1$ is an envelope-dependent constant on the order of unity ($B_0 \approx 0.94$ for a Gaussian envelope). For a 35 fs, 400 nm driving pulse, $\Delta I_{\max} \approx 7.5$ TW/cm^2 (1 TW $= 10^{12}$ W). The theoretical results in Figs. 1(a) and 1(b) were obtained by solving the time-dependent Schrödinger equation (TDSE) in full dimensionality and also by using the two-level atom (TLA) model of Ref. [6]. Further details for the simulations can be found in Ref. [19].

The depth of the oscillations of $w(I_{\max})$ records the population loss from the Rydberg state between t_1 and t_2, as illustrated in Figs. 1(b) and 1(c). Thus, following the Stückelberg oscillations vs $I_{\max}$, which controls the delay $\tau_D = t_2 - t_1$ between the resonances, allows one to measure the ionization lifetimes of strongly driven Rydberg states. Since the Stückelberg oscillations are mapped onto the final population of the Rydberg states, they can be observed via the intensity of the characteristic free-induction decay (FID) lines, which are proportional to these populations. Thus, observation of the free-induction decay after the laser pulse enables all-optical Stückelberg oscillations spectroscopy of strongly driven Rydberg states during the laser pulse. We have implemented this idea experimentally.

In the experiment, we used a 1 kHz Ti:sapphire laser system (*SpectraPhysics SpitfireAce*) which delivered 35 fs pulses (FWHM) centered around 795 nm with pulse energies up to 4 mJ. A laser beam attenuator at the system output enabled high-resolution intensity control without changing the beam propagation direction. The radiation was further frequency-doubled in a type-I β-barium-borate (BBO) crystal yielding radiation centered at 397 nm, and further focused with f/100 mirror down to 30 μm (at $1/e^2$) into a 1.2-mm-long gas-cell filled with argon at a pressure of ≈3 mbar.

The resulting extreme ultraviolet (XUV) radiation was analyzed by an XUV spectrometer [20] consisting of a toroidal mirror and a gold-coated grating. The distances between the spectrometer parts were carefully adjusted to obtain a 1 : 1 image of the interaction area. A microchannel plate together with a phosphorus screen was placed in the image plane, converting the XUV radiation into the visible range, which was recorded with a complementary metal-oxide-semiconductor (CMOS) camera.

The XUV radiation was recorded and analyzed as a function of incident laser intensity. Figure 2 shows the typical spectrum generated with laser peak intensity of ≈80 TW/cm^2. The broad peak at 15.65 eV corresponds to the fifth harmonic of the driver, while much narrower peaks labeled A–D can be assigned to the dipole-allowed free-induction decay (FID) from 4d, 5d, 6d, 6s, 7s, and 8s states to the ground 3p state, based on the argon level diagram [21]. They are split due to the spin-orbit coupling in the Ar^+ ion ($^2P_{1/2}$ and $^2P_{3/2}$ states; see Fig. 2). The lines A, B, C, D in Fig. 2 include

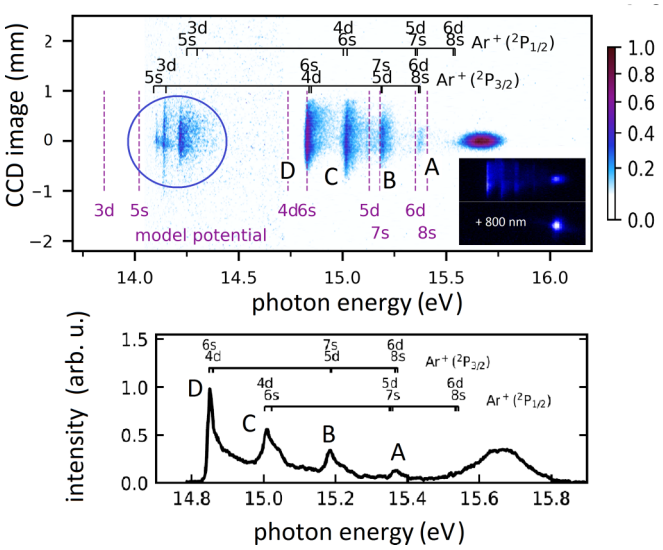

FIG. 2. Spectrum generated at a peak intensity of 80 TW/cm^2. The broad peak centered around 15.65 eV corresponds to the fifth harmonic, while the four narrow lines (A–D) originate from FID of excited states associated with spin-orbit components of the Ar^+ ion ($^2P_{1/2}$ and $^2P_{3/2}$). The FID lines from 3d and 5s states (inside the blue circle) become prominent at higher intensities (100–120 TW/cm^2). The FID lines vanish if a weak 800 nm probe pulse spatially overlaps with the 400 nm pump beam, as shown in inset of the upper panel.

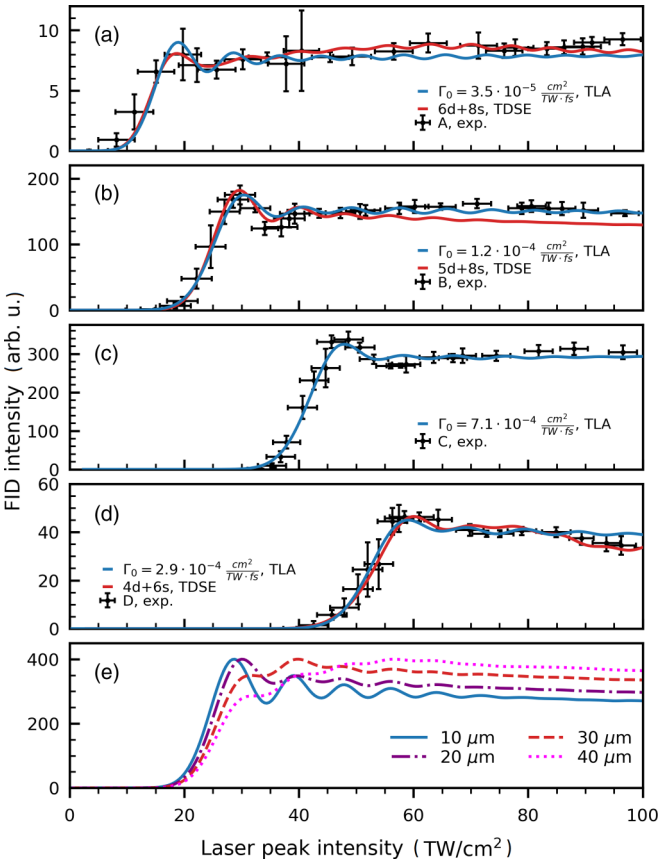

FIG. 3. Intensity of radiation emitted from FID as function of laser intensity obtained in the experiment (black circles with vertical and horizontal lines representing double standard deviations) together with results of the volume-averaged simulations for the two-level atom model (blue line) and TDSE (red line). Panel (e) shows the calculated FID intensities of the radiation composed of $4d + 6s$ states for various slit sizes as parameter (see Ref. [19]).

contributions from at least two unresolved FID transitions with photon energies 14.85, 15.01, 15.18, and 15.36 eV.

We have checked that the A–D lines disappear if a weak 800 nm probe pulse follows the driver pulse, depleting the Rydberg states and thus quenching the free-induction decay. Additional lines corresponding to the FID from the spin-orbit-split 3d and 5s states, marked with a blue circle (see Fig. 2), are absent at lower driver intensities and appear one after another upon increasing the driver intensity. Indeed, as the driver intensity increases, the AC Stark shift moves lower excited states in and out of the five-photon resonance with the ground state, thus progressively populating lower-lying states (see Fig. 3).

Figure 3 shows the intensity of each of the FID lines as a function of laser intensity. The FID radiation only appears once the AC Stark shift is sufficient to lift the corresponding state up into resonance. After prompt rise, the FID signal decreases and exhibits clear damped oscillations at higher laser intensities. Observing the oscillations confirms that the population excited on the raising edge of the pulse survives through the field maximum until the second resonance on the falling edge.

To get better insight into our experimental results, we performed single-atom TDSE simulations (further details can be found in Ref. [19]), see Fig. 4. As expected, the populations of the excited states increase with intensity, starting with the highest 8s state and progressing to the lowest 4d, and oscillates rapidly as a function of the peak intensity for each state. Almost complete destructive interference occurs in the case of 4d at 60 TW/cm^2 and 7s at 31 TW/cm^2 states, whereas the depth of the oscillation in the 5d state is rather moderate. High contrast of the Stückelberg oscillations for the 4d, 5d, 6d, and 8s Rydberg states demonstrates that hardly any ionization occurs from these states even at the intensities $I \approx 100$ TW/cm^2, with 4d, 6d, and 8s being the most striking examples, providing a direct signature of atomic stabilization in Rydberg states.

In Figs. 1(b) and 1(c) we find excellent agreement between the results of the simple two-level model [6,22] and the results of the TDSE simulations. This agreement allows us to extract lifetimes $1/\Gamma_0$ of the corresponding Rydberg states. For example, for the 6s state, which shows rapidly decreasing oscillation contrast with laser intensity, we find the lifetime of $1/\Gamma_0 \approx 15$ fs for $I_0 = 50$ TW/cm^2, which decreases to ≈9 fs at 65 TW/cm^2. The d states remain extremely stable even at high intensities, with lifetimes exceeding the pulse duration.

To contrast these conclusions for the single-atom models against our experimental observations, we must account for the focal averaging and the macroscopic phase-matching of the FID radiation. While the thin gas cell, the low gas pressure, and the focal geometry allow for simple coherent addition of local FID emissions inside the interaction volume with negligible phase mismatch, the intensity distribution in the focus plays a crucial role. This is not unexpected: the Stückelberg

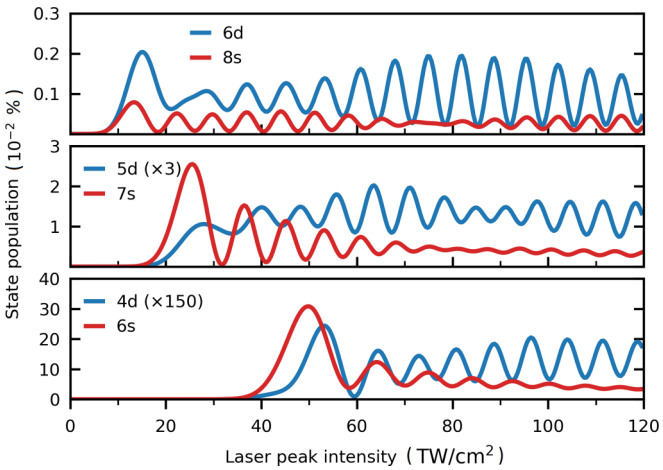

FIG. 4. Calculated populations of the atomic states as a function of peak laser intensity of the 40 fs driving pulse. See text for details.

oscillations were initially judged to be completely obscured by the focal averaging [6]. Their observation in the few-photon regime [13] required an ingenious experimental setup mapping the beam position—and thus the peak intensity—onto the detector arrival time.

We model volume effects by integrating both the TDSE results and the results of the two-level model over the gas cell and the spatial beam intensity distribution. The resulting radiation is calculated as a coherent sum of all dipoles, emitting in the forward direction in the far-field limit, with a spatially dependent phase and the intrinsic atomic phase. The crucial aspect of the experimental setup, which enables observation of the Stückelberg oscillations, is the combination of the toroidal mirror and a planar grating used at grazing incidence in the spectrometer. This setup excludes a significant part of the divergent FID beam [23] in the horizontal plane and effectively introduces a spatial filter placed in the object or the image plane. Without such an effective aperture, the spatial averaging would have suppressed the oscillations [13]. Further details of the volume averaging can be found in Ref. [19]. The results of the volume-averaged simulations for two level atom model and the TDSE are shown in Fig. 3. To determine the effective slit size imposed in the experiment, we used the TDSE results and fit them to the experimental data using the slit size as a free parameter, yielding an effective size of 17 μm with excellent agreement between the model and the experiment.

In the next step, we determined the lifetimes (ionization rates) of the corresponding levels by fitting the results of the two-level model to the experimental data with Γ_0 as parameter, which are listed in Fig. 3. The resulting ionization rate for $4d + 6s$ state [Fig. 3(c)] is in close agreement with the rate obtained by comparing the TDSE and the model results for a single atom, see Fig. 1(b) ($6s$ state), even though the two states contributing to the experimental signal are unresolved in the experiment. However, the ionization rate for $5d + 7s$ states deviates by an order of magnitude from the rate obtained for the single $7s$ state by comparing the two-level model with the TDSE result in Fig. 1(b). In this case, the amplitude of the Stückelberg oscillations observed in the experiments could be affected by the experimental conditions, including contributions from unresolved s and d states.

The effects of the aperture on the simulated FID emission are illustrated in Fig. 3(e). The interference is barely discernible if the whole target volume is allowed to contribute (pink dotted line). Moreover, in that case the intensity of the FID radiation increases monotonically with laser intensity for all states (data not shown). By decreasing the diameter of the aperture to values smaller than the beam waist at the focus ($2w_0 = 60$ μm) the interference becomes ever more visible. For the spatial filter in the form of a slit our modeling in Fig. 3(e) predicts that the smaller the slit size, the more visible the Stückelberg oscillations are [19]. It is thus feasible to minimize the effects of spatial averaging through spatial filtering to the radiation.

As discussed above, it is possible to extract the ionization rates from the contrast of the Stückelberg oscillations, which we have done both for the single-atom TDSE results and using the two-level model and comparing with the experiment. Clearly, volume-averaging effects complicate inversion of the experimental data. Thus, further improvement of the experimental setup is required to perform more accurate reconstruction of the intensity-dependent lifetimes. In addition to reducing the volume-averaging effects, the method would clearly benefit from improving the resolution of the spectrometer to resolve FID from each Rydberg state.

To summarize, the Stückelberg oscillations in the Freeman resonances arising during strong-field ionization have been observed in the free-induction decay, using an all-optical setup. The aperture introduced by the setup allows one to keep the volume-averaging effects under control and is the key for the success of this measurement. Our work shows that Stückelberg interference can be used as a sensitive spectroscopic tool to analyze the behavior of Rydberg states in strong laser fields. Good agreement of the experiment with both simple two-level model and accurate numerical simulations confirms the feasibility of Ramsey-type "Stückelberg spectroscopy" of strongly driven Rydberg states via their free-induction decay.

N.Z., U.B., and M.I. acknowledge financial support from the DFG QUTIF Grant IV No. 152/6-2.

APPENDIX A: INTENSITY POSITIONS OF STÜCKELBERG MAXIMA: STATIONARY-PHASE ANALYSIS

We consider the usual perturbation-theory expression for the wave function response in the presence of a time-dependent perturbation $\hat{V}_t$ due to the laser field [24]:

$$|\Psi(t)\rangle = |\Psi_0\rangle - i\int_{t_0}^{t} dt' \hat{U}(t,t')\hat{V}_{t'}|\Psi_0\rangle, \tag{A1}$$

where the zero energy has been chosen to coincide with the field-free energy of the initial (ground) state $|\Psi_0\rangle$, so that no time-dependent phase is accumulated by this term. In the velocity-gauge and dipole approximation, the perturbation $\hat{V}_t$ is given by (atomic units)

$$\hat{V}_t = e\vec{A}_t \cdot \hat{\nabla} + \frac{e^2}{2}A_t^2, \tag{A2}$$

where $e = -1$ is the electron charge, $-i\vec{\nabla}$ is the momentum operator, and $\vec{A}_t$ is the vector-potential at the coordinate origin:

$$\vec{A}_t = \omega^{-1}\vec{F}_0 f(t)\cos\omega t. \tag{A3}$$

In Eq. (A3) we assume that the laser field is linearly polarized with the slowly varying temporal envelope $f(t)$. We neglect the effects associated with the carrier-envelope phase (CEP) due to the multicycle nature of the pulses.

To describe the behavior of the Rydberg states, we choose to approximate the full propagator $\hat{U}(t,t')$ by the zeroth-order Kramers-Henneberger propagator [25], $\hat{U} \approx \hat{U}_{\mathrm{KH},0}$. After transforming back into the laboratory frame of reference, it is given by

$$\hat{U}_{\mathrm{KH},0}(t,t')|\chi_\kappa(\vec{r}-\vec{\alpha}_{t'})\rangle = |\chi_\kappa(\vec{r}-\vec{\alpha}_t)\rangle^{-\epsilon_\kappa(t-t')-\frac{1}{2}\int_{t'}^{t}A_\tau^2 d\tau}, \tag{A4}$$

where χ_κ and ϵ_κ are the solutions of the time-independent Schrödinger equation in the zeroth-order Kramers-Henneberger potential $v_{\mathrm{KH},0}$:

$$\left(-\frac{1}{2}\hat{\Delta} + v_{\mathrm{KH},0}\right)\chi_\kappa = \epsilon_\kappa\chi_\kappa, \tag{A5}$$

$$v_{\mathrm{KH},0} = \frac{\omega}{2\pi}\int_0^{\frac{2\pi}{\omega}} v(\vec{r}+\vec{\alpha}_\tau)d\tau, \tag{A6}$$

where $\vec{\alpha}_t$ is the displacement of a classical electron with zero drift momentum:

$$\vec{\alpha}_t = -e\int_{-\infty}^{t}\vec{A}_\tau d\tau. \tag{A7}$$

Inserting Eq. (A4) into Eq. (A1) and projecting the result onto $[|\chi_\kappa(\vec{r}-\alpha_t)\rangle^{-\epsilon_\kappa t}]^*$, we obtain the excitation amplitude a_κ for the state κ:

$$a_\kappa = e\int_{t_0}^{t} dt' e^{\epsilon_\kappa t' - \frac{1}{2}\int_{t'}^{t}A_\tau^2 d\tau}\vec{A}_{t'}\cdot\langle\chi_\kappa(\vec{r}-\vec{\alpha}_{t'})|\hat{\nabla}|\Psi_0\rangle, \tag{A8}$$

where we used the strong-orthogonality condition to eliminate the matrix element of $A_{t'}^2$ in Eq. (A8). Because we are only interested in the position of constructive interferences (maxima) of a_κ, it is sufficient to examine the rapidly oscillating exponential part of the integral (A8). We will, however, note that, because $\langle\chi_\kappa(\vec{r}-\vec{\alpha}_{t'})|$ is not an eigenfunction of a centrosymmetric potential, the usual one-photon atomic angular-momentum selection rules do not apply to Eq. (A8); excitations to Kramers-Henneberger states which adiabatically correlate to arbitrary zero-field L values are allowed. This reflects the distortion of the states by the dressing laser field, or, in other words, laser-induced coupling between the field-free Rydberg states, which allows the population transferred to one field-free Rydberg state via standard transitions to flow to other Rydberg states with different angular momenta.

Following the standard stationary-phase analysis procedure [26,27], we obtain two stationary points of the integral per laser cycle, allowing us to approximate Eq. (A8) by a sum over the stationary points [26,27]:

$$a_\kappa \approx \sum_n C_n^{\phi_n}, \tag{A9}$$

$$\phi_n = \epsilon_\kappa t_n - \frac{1}{2}\int_{t_n}^{t} A_\tau^2 d\tau, \tag{A10}$$

$$t_n = t_{n,\mathrm{r}} + t_{n,\mathrm{i}}, \tag{A11}$$

$$\omega t_{n,\mathrm{r}} = \frac{\pi}{2} + \pi n, \tag{A12}$$

$$\omega t_{n,\mathrm{i}} = \gamma_n, \tag{A13}$$

$$\gamma_n = \sqrt{\frac{\epsilon_\kappa}{2U_{\mathrm{p},n}}}, \tag{A14}$$

$$U_{\mathrm{p},n} = \frac{F_0^2}{4\omega^2}f^2(t_{n,\mathrm{r}}). \tag{A15}$$

Equation (A9) is the strong-field excitation analog of the usual strong-field approximation (SFA) results for strong-field ionization and high-harmonics generation processes [26,27]. The prefactors C_n encompass all the contributions of the slowly varying terms in the integral (A8), but can otherwise be left unspecified in our analysis. From the definition of the $\langle\chi_\kappa(\vec{r}-\vec{\alpha}_{t_n})|\hat{\nabla}|\Psi_0\rangle$ matrix elements, we expect the prefactors C_{2n} and C_{2n+1}, which correspond to the similar free-electron position α_{t_n} (the outer and inner turning points, respectively), to form slowly varying progressions, while the prefactors separated by one half of the driver period (C_n and C_{n+1}) can be significantly different, depending on the nature of the electronic states involved.

The overall amplitude (A9) exhibit two types of constructive interferences: cycle to cycle and long term. The cycle-to-cycle constructive interference arises when

$$\mathrm{Re}(\phi_{n+2} - \phi_n) = 2\pi m, \tag{A16}$$

where m is an integer. Substituting Eqs. (A10)–(A12) and taking the A_τ^2 integral using the trapezoidal rule, we obtain the cycle-to-cycle interference condition:

$$\epsilon_\kappa + \tfrac{1}{2}(U_{\mathrm{p},n} + U_{\mathrm{p},n+2}) = \omega m, \tag{A17}$$

which corresponds to the m-photon resonance between the ground state and the Stark-shifted Rydberg state [28]. This condition is satisfied twice: once on the raising edge, and the second time on the falling edge of the pulse envelope (see Fig. 1 of the main text). From Eq. (A17), the cycle-to-cycle resonance condition re-occurs at the peak laser field intensities separated by [28]

$$\Delta I_{\mathrm{peak}} = \Delta\left(F_0^2\right) \approx 4\omega^3. \tag{A18}$$

For the 400 nm driver field, this corresponds to ≈210 TW/cm^2, which is outside the experimental intensity range. We therefore expect at most one cycle-to-cycle constructive interference per target state in our experiment.

In order to evaluate the positions of the long-time constructive interferences it is necessary to specify the field envelope. We will assume that it is Gaussian, with the full width at half maximum duration (power) of τ_{FWHM}:

$$f(t) = \exp\left(-\frac{2\ln 2}{\tau_{\mathrm{FWHM}}^2}t^2\right). \tag{A19}$$

For this envelope, the cycle-to-cycle resonance condition (A17) is satisfied at $\pm t_m$, with t_m given by

$$t_m = \frac{\tau_{\mathrm{FWHM}}}{2\sqrt{\ln 2}}\sqrt{\ln\frac{U_{p,\mathrm{peak}}}{m\omega - \epsilon_\kappa}}, \tag{A20}$$

where the peak ponderomotive potential is given by

$$U_{p,\mathrm{peak}} = \frac{F_0^2}{4\omega^2}. \tag{A21}$$

The constructive resonance condition is then given by

$$\phi_{t_m} - \phi_{-t_m} = 2t_m\epsilon_\kappa + \frac{1}{2}\int_{-t_m}^{+t_m} A_\tau^2 d\tau = 2\pi l, \tag{A22}$$

where l is an integer.

The transcendental equation (A22) does not have nontrivial closed-form solutions. However, evaluating the A_τ^2 integral in the slowly varying envelope approximation and collecting the slowly varying functions of $U_{p,\mathrm{peak}}$ on the right-hand side, we obtain

$$U_{p,\mathrm{peak}} = \frac{1}{\zeta}\left(l\sqrt{\frac{4\ln 2}{\pi}}\frac{2\pi}{\tau_{\mathrm{FWHM}}} - \frac{2\epsilon_\kappa}{\sqrt{\pi}}\zeta\right), \tag{A23}$$

$$\zeta = \sqrt{\ln\frac{U_{p,\mathrm{peak}}}{m\omega - \epsilon_\kappa}}. \tag{A24}$$

Equation (A23) can be readily evaluated numerically for all m, l using fixed-point iterations. Furthermore, in the high-intensity limit ($U_{p,\mathrm{peak}} \gg m\omega - \epsilon_\kappa$) $\zeta \to 1$, and the intensity spacing between the consecutive constructive interferences is determined by the first term in Eq. (A24):

$$\Delta I_{\mathrm{peak}} \approx 4B_0\omega^2\frac{2\pi}{\tau_{\mathrm{FWHM}}}, \tag{A25}$$

$$B_0 = \sqrt{\frac{4\ln 2}{\pi}} \approx 0.94. \tag{A26}$$

Thus, the maxima are expected to repeat at intensities proportional to the driver bandwidth $\frac{2\pi}{\tau_{\mathrm{FWHM}}}$ and inversely proportional to the square of its wavelength λ ($\omega = \frac{2\pi c}{\lambda}$). For $\lambda = 400$ nm and $\tau_{\mathrm{FWHM}} = 35$ fs, we expect $\Delta I_{\mathrm{peak}} \approx 7.5$ TW/cm^2, which is consistent with the TDSE results shown in Fig. 1 of the main text.

APPENDIX B: NUMERICAL DETAILS

The TDSE implementation is described in Ref. [29]. We numerically solve the one-electron time-dependent Schrödinger equation (TDSE) in spherical coordinates by applying the dipole approximation in the velocity gauge. The exciting laser pulse at 400 nm central wavelength has a Gaussian envelope with 40 fs FWHM, linearly polarized along the z direction. It is smoothly turned off, 66.5 fs measured from the pulse center. The argon atom is modeled with the potential described in Ref. [30]. The simulation includes angular momenta up to $L_{\max} = 15$. The radial grid increases uniformly from 0.039 Bohr up to 1.961 Bohr in 0.038 Bohr steps and continues logarithmically from 2 Bohr to 15.07 Bohr. From this point, the grid again increases uniformly in steps of 0.3 Bohr to 119.17 Bohr. An absorbing boundary [31] is applied at the outer edge. The calculations were performed for laser peak intensities ranging from 0.4 to 120 TW/cm^2 in steps of 0.4 TW/cm^2.

The analytical model [6] includes the ground state and the excited state, the latter undergoing both a ponderomotive energy shift and ionization decay. The excited and the ground states are coupled via an N-photon matrix element $V_n \propto I^{N/2}$ (I is the laser intensity), for our case of $N \geqslant 4$ the exact value of the matrix element only determines the overall scale and does not affect the modulation contrast. The ionization rate is $\Gamma(t) = \Gamma_0(I/I_0)$, $I_0 = 60$ TW/cm^2, with Γ_0 varied to calibrate the Stückelberg oscillations obtained in the model against the TDSE, thus finding the ionization rate as shown in Figs. 1(b) and 1(c). We have used a Gaussian laser pulse with 40 fs duration (FWHM) centered at 400 nm, and ran both the TDSE and the two-level model simulations for peak intensities from $I_0 = 0.4$ TW/cm^2 to $I_0 = 120$ TW/cm^2.

The fields used in the simulation are intense enough to excite from both p_0 and $p_\pm$ ground states of argon. However, the excited-state populations resulting from excitation from $p_\pm$ states at the end of the simulation are lower by a factor of ≈30 compared with excitation from p_0 and therefore neglected in the discussion.

APPENDIX C: FOCAL VOLUME AVERAGING

To compare the results of the TDSE simulation with the experimental data we have to consider the effects of spatial volume averaging. We therefore map the results of the TDSE to the intensity distribution of a Gaussian beam

$$I(r,z) = I_0\frac{w_0^2}{w^2(z)}e^{-\frac{2r^2}{w^2(z)}}, \tag{C1}$$

with $w(z) = w_0[1 + (\frac{z}{z_R})^2]^{1/2}$ and w_0 denoting the width and z_R the Rayleigh length.

We discretize the volume utilizing the cylindrical symmetry on the z and r axes ($\Delta z = 20$ μm, $\Delta r = 1$ μm) and create an array of atomic dipoles: for each peak intensity I_0 in the experiment we obtain amplitudes $a(I_0, r_i, z_i)$ and phase $\phi_{\mathrm{at}}(I_0, r_i, z_i)$ at each position (r_i, z_i) on the grid directly from the results of the TDSE. We later account for the full volume by integrating over all azimuthal angles φ. Additionally, each dipole acquires a geometrical phase:

$$\phi_{\mathrm{geom}}(z, z_i, r_i) = -ik_L(z - z_i) - ik_L\frac{r_i^2}{2R(z_i)} + i\psi(z_i), \tag{C2}$$

where k_L denotes the wave number of the laser, $R(z_i) = z_i[1 + (z_R^2/z^2)]$. the curvature of the laser wavefront at position z_i and $\psi(z) = \arctan(\frac{z}{z_R})$ the Gouy phase. The electric field radiated by the dipoles in the far-field limit at distance L reads

$$F(t; I_0, r_i, z_i) \propto a(I_0, r_i, z_i)e^{\phi_{\mathrm{at}}(I_0,r_i,z_i)}e^{\phi_{\mathrm{geom}}(L,z_i,r_i)}e^{ik_{FID}(L-z_i)} \times e^{-i\omega_{\mathrm{FID}}t}, \tag{C3}$$

where k_{FID} is the wave number of the FID radiation and we consider only emission in the forward direction since $L \gg 2w_0$. To calculate the signal $S(I_0)$ measured at the center

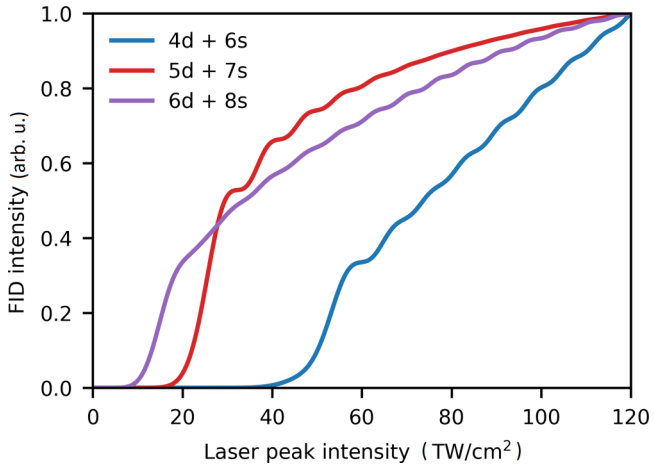

FIG. 5. Spatial averages of FID radiation obtained by modeling, considering the full focal volume.

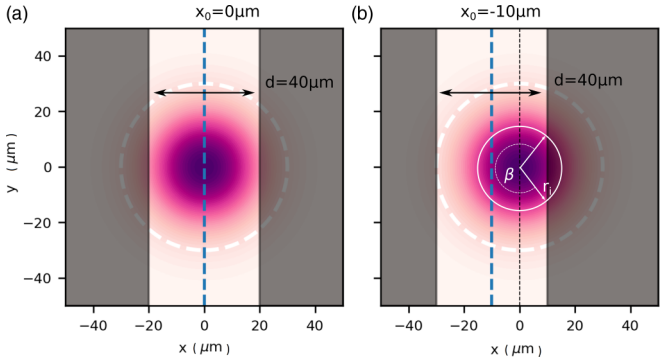

FIG. 6. Modeling of spatial filtering with a slit (black shaded areas). The Gaussian intensity profile of the laser is represented by the red-purple colormap, where a darker color means higher intensity. The black dashed line denotes the center of the intensity distribution with respect to x, the white dashed circle marks the width w_0 of the Gaussian beam. (a) Slit centered according to the intensity maximum of the laser and an aperture $d = 40\ \mu$m. (b) Slit positioned off-center at $x_0 = -10\ \mu$m and an aperture of $d = 40\ \mu$m. The purple dashed line marks the center of the slit.

of the detector as a function of peak intensity of the laser, we coherently add the radiation from all dipoles along the z direction (forward direction) and incoherently along the r direction (assuming emission only in forward direction)

$$S(I_0) = \sum_{r_i} 2\pi r_i \left| \sum_{z_i} F(I_0, r_i, z_i) \right|^2, \tag{C4}$$

where the factor $2\pi r_i = \int_0^{2\pi} d\varphi r_i$ originates from the azimuthal integration. Note that we dropped the time dependence of the electric field since the detector is slow and realistic measurements average over many cycles.

The experimentally observed spectral peaks in each case consist of radiation of at least two FID transitions which cannot be resolved by the XUV spectrometer. We account for this in the modeling by adding the signal of each contribution of the corresponding transitions weighted by its Einstein coefficient.

APPENDIX D: SPATIAL FILTERING

Focal volume averaging as presented in Appendix C results in a signal, where all Stückelberg oscillations are "washed out." Figure 5 shows the graphs that we obtain from the TDSE and the focal volume averaging discussed in Appendix C. Compared with the results of single-atom modeling (Fig. 4) the oscillations are far less pronounced. This is also true compared with the experimental results (Fig. 3). We identified the reason for this to lie in geometrical restrictions in the experiment, which prevent the entire FID radiation from arriving at the detector. Due to grazing incidence (at a quite extreme angle) on the spectrometer grating, the FID beam is partly horizontally truncated. Without such truncation, the output of the FID lines demonstrate a monotonic growth as shown in Fig. 5 and as observed in the experiment [11]. To model this geometry, we consider a spatial filter in the form of a slit that can be applied to the radiation source, effectively truncating the generation volume. Figure 6 shows an illustration of the placement of the slit (dark, shaded) relative to the intensity distribution in the transverse plane. The parameters characterizing the slit are its aperture d and the placement x_0 of its center along the horizontal axis.

Clearly, the cylindrical symmetry of the generation medium is broken in this case, so that the integration over azimuthal angles ϕ has to be modified to account for the truncation of the generation volume. The signal then reads

$$S(I_0) = \sum_{r_i} w(r_i) \left| \sum_{z_i} F(I_0, r_i, z_i) \right|^2, \tag{D1}$$

where the weight factor $w(r_i)$ reads

$$w(r_i) = \int_0^{\beta} d\varphi\ r_i, \tag{D2}$$

$$\beta = \begin{cases} 2\pi, & r_i < \frac{d}{2} - x_0 \\ 2\pi - 2\arccos\left(\frac{\frac{d}{2} - x_0}{r_i}\right), & \frac{d}{2} - x_0 < r_i < \frac{d}{2} + x_0 \\ 2\pi - 2\left[\arccos\left(\frac{\frac{d}{2} - x_0}{r_i}\right) + \arccos\left(\frac{\frac{d}{2} + x_0}{r_i}\right)\right], & r_i > \frac{d}{2} + x_0. \end{cases} \tag{D3}$$

To find the best fit of the model to the experimental data, we run a parameter search over x_0 and d. The results for the best fit are shown in Fig. 3 in the article.

[1] P. Agostini, P. Breger, A. L'Huillier, H. G. Muller, G. Petite, A. Antonetti, and A. Migus, Giant Stark Shifts in Multiphoton Ionization, Phys. Rev. Lett. **63**, 2208 (1989).

[2] P. B. Corkum and F. Krausz, Attosecond science, Nat. Phys. **3**, 381 (2007).

[3] R. R. Freeman, P. H. Bucksbaum, H. Milchberg, S. Darack, D. Schumacher, and M. E. Geusic, Above-Threshold Ionization with Subpicosecond Laser Pulses, Phys. Rev. Lett. **59**, 1092 (1987).

[4] M. P. de Boer and H. G. Muller, Observation of Large Populations in Excited States After Short-Pulse Multiphoton Ionization, Phys. Rev. Lett. **68**, 2747 (1992).

[5] G. N. Gibson, R. R. Freeman, and T. J. McIlrath, Verification of the Dominant Role of Resonant Enhancement in Short-Pulse Multiphoton Ionization, Phys. Rev. Lett. **69**, 1904 (1992).

[6] G. N. Gibson, R. R. Freeman, T. J. McIlrath, and H. G. Muller, Excitation and ionization dynamics in short-pulse multiphoton ionization, Phys. Rev. A **49**, 3870 (1994).

[7] S. Camp, K. J. Schafer, and M. B. Gaarde, Interplay between resonant enhancement and quantum path dynamics in harmonic generation in helium, Phys. Rev. A **92**, 013404 (2015).

[8] T. Nubbemeyer, K. Gorling, A. Saenz, U. Eichmann, and W. Sandner, Strong-field Tunneling Without Ionization, Phys. Rev. Lett. **101**, 233001 (2008).

[9] U. Eichmann, A. Saenz, S. Eilzer, T. Nubbemeyer, and W. Sandner, Observing Rydberg Atoms to Survive Intense Laser Fields, Phys. Rev. Lett. **110**, 203002 (2013).

[10] G. L. Yudin and M. Y. Ivanov, Physics of correlated double ionization of atoms in intense laser fields: Quasistatic tunneling limit, Phys. Rev. A **63**, 033404 (2001).

[11] M. Chini, X. Wang, Y. Cheng, H. Wang, Y. Wu, E. Cunningham, P.-C. Li, J. Heslar, D. A. Telnov, S.-I. Chu, and Z. Chang, Coherent phase-matched VUV generation by field-controlled bound states, Nat. Photonics **8**, 437 (2014).

[12] S. V. Popruzhenko, Quantum theory of strong-field frustrated tunneling, J. Phys. B: At., Mol. Opt. Phys. **51**, 014002 (2017).

[13] R. R. Jones, Interference Effects in the Multiphoton Ionization of Sodium, Phys. Rev. Lett. **74**, 1091 (1995).

[14] E. C. G. Stückelberg, Theory of Inelastic Collisions between Atoms, Helv. Phys. Acta **5**, 369 (1932).

[15] L. Sirko, S. Yoakum, A. Haffmans, and P. M. Koch, Microwave-driven He Rydberg atoms: Floquet-state degeneracy lifted by a second frequency, Stückelberg oscillations, and their destruction by added noise, Phys. Rev. A **47**, R782 (1993).

[16] M. Baghery, U. Saalmann, and J. M. Rost, Essential Conditions for Dynamic Interference, Phys. Rev. Lett. **118**, 143202 (2017).

[17] Q.-C. Ning, U. Saalmann, and J. M. Rost, Electron Dynamics Driven by Light-Pulse Derivatives, Phys. Rev. Lett. **120**, 033203 (2018).

[18] S. N. Shevchenko, S. Ashhab, and F. Nori, Landau–Zener-Stückelberg interferometry, Phys. Rep. **492**, 1 (2010).

[19] See Appendix.

[20] D. S. Brambila, A. Husakou, M. Ivanov, and N. Zhavoronkov, On-target diagnosing of few-cycle pulses by high-order-harmonic generation, Phys. Rev. A **96**, 063825 (2017).

[21] K. Yoshino, Absorption spectrum of the argon atom in the vacuum-ultraviolet region, J. Opt. Soc. Am. **60**, 1220 (1970).

[22] C. R. Holt, M. G. Raymer, and W. P. Reinhardt, Time dependences of two-, three-, and four-photon ionization of atomic hydrogen in the ground $1\,^2S$ and metastable $2\,^2S$ states, Phys. Rev. A **27**, 2971 (1983).

[23] S. Beaulieu, S. Camp, D. Descamps, A. Comby, V. Wanie, S. Petit, F. Légaré, K. J. Schafer, M. B. Gaarde, F. Catoire, and Y. Mairesse, Role of Excited States In High-order Harmonic Generation, Phys. Rev. Lett. **117**, 203001 (2016).

[24] A. Becker and F. M. H. Faisal, Intense-field many-body *S*-matrix theory, J. Phys. B **38**, R1 (2005).

[25] W. C. Henneberger, Perturbation Method for Atoms in Intense Light Beams, Phys. Rev. Lett. **21**, 838 (1968).

[26] O. Smirnova and M. Ivanov, Multielectron high harmonic generation: Simple man on a complex plane, in *Attosecond and XUV Physics*, edited by T. Schultz and M. Vrakking (Wiley, 2014), Chap. 7.

[27] O. Smirnova and M. Ivanov, Multielectron High Harmonic Generation: Simple man on a complex plane, in *Attosecond and XUV Physics: Ultrafast Dynamics and Spectroscopy*, edited by T. Schultz and M. Vrakking (Wiley-VCH, Weinheim, 2014), p. 201, Sec. 7.

[28] H. Zimmermann, S. Patchkovskii, M. Ivanov, and U. Eichmann, Unified Time and Frequency Picture of Ultrafast Atomic Excitation in Strong Laser Fields, Phys. Rev. Lett. **118**, 013003 (2017).

[29] S. Patchkovskii and H. G. Muller, Simple, accurate, and efficient implementation of 1-electron atomic time-dependent Schrödinger equation in spherical coordinates, Comput. Phys. Commun. **199**, 153 (2016).

[30] X. M. Tong and C. D. Lin, Empirical formula for static field ionization rates of atoms and molecules by lasers in the barrier-suppression regime, J. Phys. B: At., Mol. Opt. Phys. **38**, 2593 (2005).

[31] D. E. Manolopoulos, Derivation and reflection properties of a transmission-free absorbing potential, J. Chem. Phys. **117**, 9552 (2002).